npj | 2D materials and applications

www.nature.com/npj2dmaterials

ARTICLE OPEN

Check for updates

A candidate material $EuSn_2As_2$-based terahertz direct detection and imaging

Changlong Liu[1,2,6], Yi Liu[3,6], Zhiqingzi Chen[2,6], Shi Zhang[1], Chaofan Shi[1], Guanhai Li[1,2], Xiao Yu[4], Zhiwei Xu[4], Libo Zhang[2], Wenchao Zhao[5], Xiaoshuang Chen[1,2]✉, Wei Lu[2] and Lin Wang[2]✉

Exploring the photoelectric performance of emerging materials represented by graphene, black phosphorus and transition metal dichalcogenides is attracting enormous research interest for a wide range of electronic and photonic applications. The realization of low-power consuming photodetectors with high sensitivity and fast photoresponse in the terahertz band remains one of the profound challenges in optoelectronics. In this study, a material-$EuSn_2As_2$ has been successfully implemented to realize highly sensitive terahertz photodetectors. The non-equilibrium dynamics in a two-dimensional plane allow an optionally switching between different styles of direct photon-conversions: the analogous photoconductive and photovoltaic modes spontaneously supported by the intrinsic electronic system. The prototype devices exhibited excellent sensitivity of 0.2–1.6 A/W (0.3–2.4 kV/W) from 0.02 to 0.30 THz at room temperature, corresponding to a noise-equivalent power <30pW/$Hz^{0.5}$ and a fast response time <16 μs. The versatile switching behaviour and performance of the $EuSn_2As_2$ flakes-based terahertz detectors were validated via rigorous full-dimension and imaging experiments. These results open the feasibility avenues for low-energy photoelectronic applications of $EuSn_2As_2$ material.

npj 2D Materials and Applications (2022)6:26 ; https://doi.org/10.1038/s41699-022-00301-z

INTRODUCTION

Terahertz (THz) radiation (0.1−10 THz), which connects electronics to optics, encompasses a wide band of the electromagnetic spectrum from microwaves to infrared light, and its mixed property enables broad applications, including wireless communication, spectroscopy, sensing, and imaging[1]. The emerging materials such as graphene, topological insulators, and three-dimensional Dirac systems, with low-energy electrodynamics is characterized by mass-less Dirac fermions, exhibit an intrinsically THz response[2,3]. However, THz detection based on layered two-dimensional (2D) materials like graphene[4], and black phosphorus[5] exhibits several drawbacks imposed by a slow response speed, high manufacturing costs, and the necessity of cryogenic cooling because of the strong background thermal noise at room temperature. Photodetection makes use of topological properties in system supporting gapped bulk excitation, opening feasibility of convenient platform driven by the global properties of quantum wavefunction to beyond traditional landmarks of band-structure engineering[6]. The photocurrent generation in topological insulators, mainly based on Bi_2Se_3, Bi_2Te_3 and Sb_2Te_3 materials, has been studied under different configurations such as overdamped plasma waves[7], and asymmetric scattering of topological surface states[8], with an aim to achieve a detectivity, comparable to or even exceeding that of graphene[9]. Topological semi-metallic materials such as Cd_3As_2, $MoTe_2$ and $TaIrTe_4$ have been recently introduced into the field of photoelectric detection[10]. Especially, the Berry-curvature-enhanced giant photoresponse of these semimetals enables their highly sensitivity photodetection in the technologically significant mid-infrared and THz regions. Thus, the practical applications of THz detection can be realized by exploring emerging materials with attractive properties, especially a fast and improved response to THz radiation.

The existing photodetectors generally detect high-energy photons above the bandgap energy via photoconductive or photovoltaic effect. However, detection via thermal effects such as bolometric, photothermoelectric (PTE) and pyroelectric effects can occur theoretically for any specific wavelength without the bandgap limitation. Among these photodetectors, the PTE-based detectors are considered as viable candidates for THz detection because of their simple geometry, zero-bias operation, and low power consumption. Wang et al. demonstrated[11] the PTE-based detection capability of the $EuBiSe_3$ single crystal, which exhibited a room-temperature self-powered photovoltage responsivity up to 0.59 V/W at THz frequencies, and a noise-equivalent power below 1 nW/Hz lower than reported photothermoelectric detectors by at least an order of magnitude. Recently, quantum materials[12] $EuSn_2As_2$, $MnBi_{2n}Te_{3n+1}$ and $Co_3Sn_2S_2$ have garnered significant attention because of their phenomena such as the quantum anomalous Hall effect (even at room temperature), chiral Majorana fermions and axion electrodynamics[13]. However, the photodetection capabilities of these materials have been rarely investigated, possibility because of the difficulty in manipulating their inherent properties, leading to a general consensus on their inapplicability in terahertz electronics.

In this communication, we reported the candidate material $EuSn_2As_2$–as an ideal platform to study 2D plane THz photoresponse that relates to the intrinsic electronic system. $EuSn_2As_2$ possesses an unconventional bulk band structure, in which metal states contribute significantly below the Fermi energy level while

[1]College of Physics and Optoelectronic Engineering, Hangzhou Institute for Advanced Study, University of Chinese Academy of Sciences, No. 1, Sub-Lane Xiangshan, Xihu District, 310024 Hangzhou, China. [2]State Key Laboratory of Infrared Physics, Shanghai Institute of Technical Physics, Chinese Academy of Sciences, 500 Yu-Tian Road, 200083 Shanghai, China. [3]College of Science, Zhejiang University of Technology, 310023 Hangzhou, China. [4]Zhejiang Lab, Artificial Intelligence Town, No.1818 Wenyixi Road, 311100 Hangzhou, China. [5]Department of Electronics and Information, School of Science and Engineering, Huzhou College, 313000 Huzhou, China. [6]These authors contributed equally: Changlong Liu, Yi Liu, Zhiqingzi Chen. ✉email: xschen@mail.sitp.ac.cn; wanglin@mail.sitp.ac.cn

the nonmetal states contribute significantly above the Fermi energy level[12]. The low-energy-photons absorption exhibited by $EuSn_2As_2$ is related to the low heat capacity associated with the mass-less Dirac electrons. The temperature of non-equilibrium carriers due to the THz illumination can be a strong modification of the electronic chemical potential, although some deviation may occur due to thermal excitation of electrons from the surface and bulk because of the presence of massive bulk carriers. The definite feature of an $EuSn_2As_2$-based photodetector is its strong photoresponse up to THz frequencies, followed by a flexible switching of operation with the involvement of analogous photoconductive and photovoltaic modes under the electromagnetic driven force. Based on the experimental results presented, $EuSn_2As_2$ material can be heralded as a promising candidate for realizing a highly sensitive and fast low-energy photodetection, promoting cutting-edge research and technological advancements in the field of THz optoelectronics.

RESULTS

Materials characterization

Single-crystal $EuSn_2As_2$ were synthesized by melting stoichiometric amounts of Eu: Sn: As (1.1: 20: 2) in an alumina crucible enclosed in a quartz tube jacket under 50 mTorr pressures and at 850 °C for 12 h (See the "Methods" section for details). $EuSn_2As_2$ flakes, exfoliated from the bulk part, are integrated with multiple antennas through a combination of lithography, electron-beam evaporation and lift-off processes (See Supplementary Methods), to enhance the photodetection sensitivity up to THz frequencies. The photosensitive $EuSn_2As_2$ crystal structure consists of hexagonal Eu, and As layers surrounding an Sn bi-layer as shown in Fig. 1a[14]. Similar to that observed in $EuSn_2P_2$ material[15], the results from single crystal X-ray diffraction patterns reveal $EuSn_2As_2$ crystallizes in a rhombohedral lattice with the space group $R\bar{3}m$ analogous to a well-known Bi_2Te_3 material. To elucidate the photodetection behaviour, the spectroscopy in relevant with low-energy or ground excited-states was performed to identify the capability of optical transition. The infrared reflection spectrum as shown in Fig. 1c demonstrates that $EuSn_2As_2$ material exhibits a strong absorption of up to 60% at ~5 μm of characteristic wavelength (photon energy: 240 meV). High-energy photons (energy > 240 meV) can excite electron-hole pairs and induce relaxation over the bandgap, whereas the middle energy photons (energy < 240 meV) can be strongly reflected and vanished because of the metallic state. The optical transition to the bulk states increases the absorption of photons with energy ~240 meV (wavelength ~ 5 μm) because of the scattering between the bulk and the metallic states. Further, the transmission spectrum of the $EuSn_2As_2$ single crystal in the frequency range of 0.02–3.0 THz was obtained by THz spectroscopic measurement techniques, displaying a huge transmission loss or a broadband absorption in this particular frequency regime as depicted in Fig. 1d (See Supplementary Fig. 4a, b). The spectroscopic results indicate that the excitation processes[16] shown in Fig. 1e induce the broadband absorption in $EuSn_2As_2$ material. Photons with energy higher than the bulk bandgap value can excite the electrons in the valence band to the corresponding conduction band as illustrated on the left side of Fig. 1e. For THz photons with energies within the absorption band of the metallic state of $EuSn_2As_2$, the observed enhanced absorption might be ascribed to the gapless metallic state-induced intra-Dirac-band excitation dynamics of the Dirac electrons (free-carrier absorption) as shown on the right side of Fig. 1e[17]. The visible/infrared absorption possibly originates from the bulk state, whereas the metallic state is responsible for the absorption in the microwave/THz band. To devise our detectors, the topographic atomic force microscopy (AFM) scan of derived $EuSn_2As_2$ flakes, shown in Fig. 1f, substantiates the layered feature with two thicknesses of ~1 μm and 100 nm, indicating that the exfoliation of large-areas atomically-thin layered $EuSn_2As_2$ is a challenging task. To ensure an ideal trade-off between the detector fabrication and the coupling performance, flakes with thicknesses in the range of 80–100 nm, which is roughly coincident with the out-of-plane thickness of the coupling antenna, are preferred.

Device design and characterizations

Figure 2a schematically illustrates the structure of the multiple-antenna-coupled $EuSn_2As_2$ material detectors for THz band detection at room temperature. The photosensitive area located at the intersection of the pair of crossed bow-tie antennas (similar to the four-leaf clover shape), which has a total length ($2R$) of ~400 μm and a flare angle of 45°, in resonance with 0.375 THz radiation covering the measured frequency range. The channel length (L of antenna gap) is 8 μm ($2r = 8$ μm), forming a photosensitive area of $S_a = \pi r^2 = 50.24\ \mu m^2$ (see Supplementary Fig. 3a for the detector image). Owing to the strong dipole-oscillating charges in the multiple-antenna configurations, shown in Fig. 2b, the deep-subwavelength gap ($L = 2r = 8\ \mu m \approx \lambda/3000$) between the antenna pairs behaves as a gap-capacitor charged by the THz-induced currents. The oscillating electric field, under different polarizations (0° and 45°) of the incident 0.1 THz and 0.3 THz radiation, displays an enhancement of several orders of magnitude (an enhancement of power $|E/E_0|^2 = 200$–300 times) at the gap to facilitate electromagnetic absorption by the $EuSn_2As_2$ flakes[18] (see Supplementary Figs. 1 and 2 for the local field distribution at 0.02–0.6 THz). Based on the FDTD simulation analysis, it could be inferred that a net photocurrent can flow to different directions in the antenna-coupled detectors owing to the changes of the localized field distributions in a 2D plane (x–y plane) of the material at different electromagnetic polarizations[19]. The standard behaviours of the different detection modes can be understood using the simplified model shown in Fig. 2c under low-resistance states circumstances (see Supplementary Fig. 3 for electrical characteristics). A probable explanation for the low-energy-photon absorption of $EuSn_2As_2$ materials, similar to graphene, is related to its low heat capacity associated with the mass-less Dirac electrons. The temperature of the electron bath increases significantly upon an intense THz excitation, thus resulting in a response dominated by incoherent thermal effects due to a less effective interaction between the electrons and the lattice. The increase in the electronic temperature under the THz illumination can strongly modify the electronic chemical potential[17], indicating that the excited non-equilibrium carrier's temperature (ΔT_e) is much higher than the lattice temperature (ΔT_L) under THz radiation. Consequently, a 2D potential gradient can form in the 2D photosensitive area because of the interplay between the radiation-induced heating and heat-sinking of the antenna pads. This potential gradient can trap and de-trap the non-equilibrium carriers under an applied bias voltage, resulting in a directional photocurrent $I_{ph} \sim (E_{THz}^2(t) + E_{dc}^2(t))$ with a high photoconductive gain (The photocurrent direction is the same as that of the applied bias voltage). Moreover, a non-directional photocurrent $I_{ph} \sim E_{THz}^2$ exists even in the absence of applied voltage (The direction of this non-directional photocurrent is different from that of the applied bias voltage), and is steered by the localized field, non-equilibrium carriers' distributions or the Bloch electrons scattering process described later[20].

To clarify the above-mentioned phenomenon, the current characteristics of the devices fabricated in this study, were recorded under the "ON/OFF" modulated radiation illumination as shown in Fig. 2d, e. The photocurrent (I_{ON}-I_{OFF}) is deemed to be more than 1 μA at room temperature, can even increase up to 6 μA in the absence of voltage (See Supplementary Fig. 5), revealing a broadband response in THz band irrespective of the

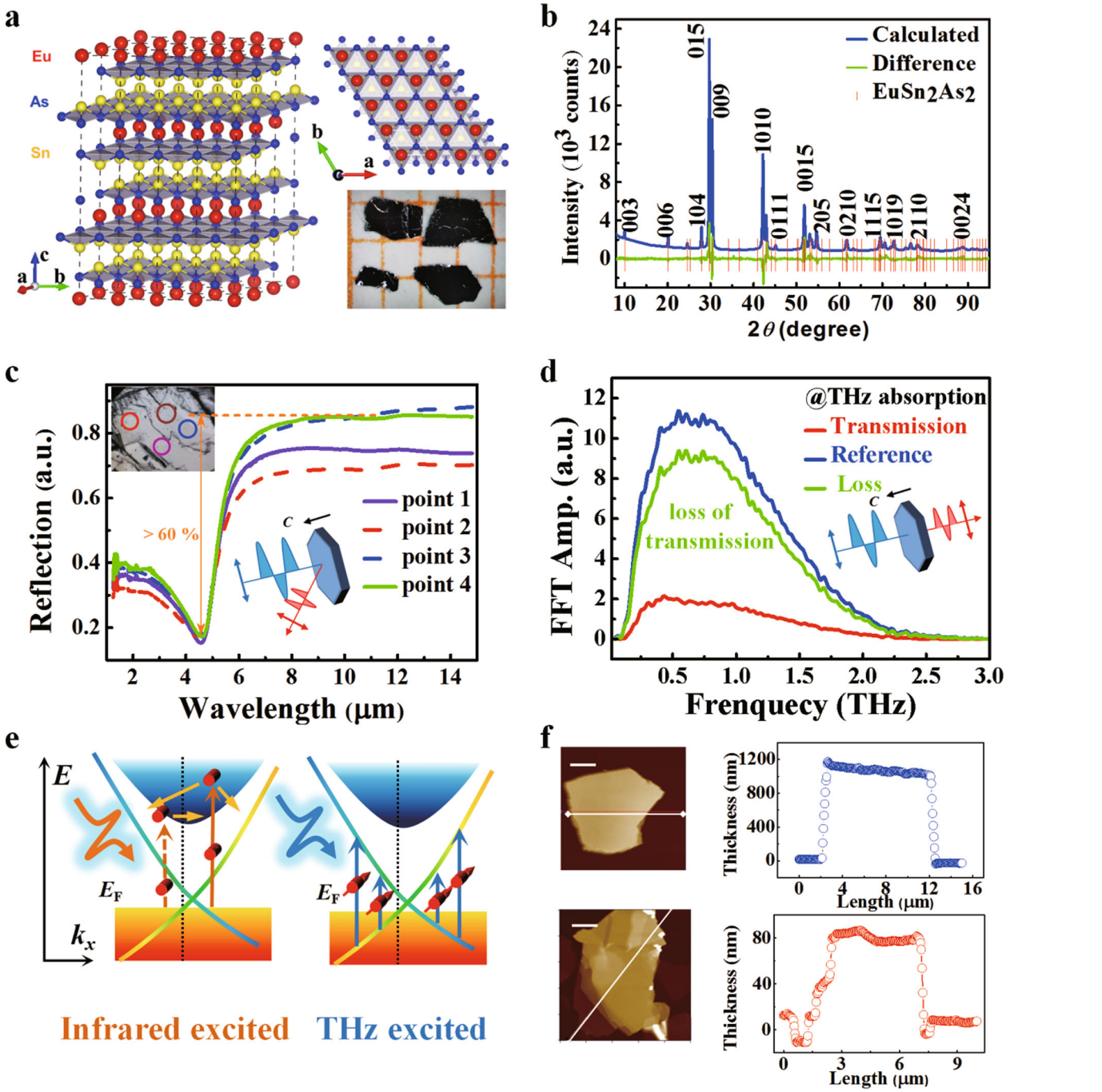

Fig. 1 Basic characterization of the single-crystal $EuSn_2As_2$. **a** Crystalline structures of $EuSn_2As_2$, in which the atoms are arranged in puckered honeycomb layers bounded together by van der Waals' forces, and an optical image at the corner with the grid length of 1 mm. **b** X-ray diffraction spectrum of the $EuSn_2As_2$ flakes with the corresponding Miller indices in parentheses. **c** Infrared reflection spectra at different sampling points. **d** The THz frequency-domain transmission spectra of with/without the samples. **e** Schematic illustration of the broadband absorption mechanisms between the bulk state and the gapless metallic state; and the blue and orange arrows indicate the low- and high-energy photons excitations, and the red solid circle indicates an electron with a spin, respectively. **f** The AFM image of $EuSn_2As_2$ flakes for device patterning indicates the thickness of the sample, and the scale bars are 4 μm (upper) and 2 μm (lower).

different coupling efficiency of the frequency-dependent antenna (See Supplementary Fig. 2 for the local field distribution). Notably, the photocurrent ($I_{ph\text{-}CA}$ or $I_{ph\text{-}DB}$) increases linearly with the increasing bias voltage (U_{CA} or U_{DB}) at 0.03 THz, 0.09 THz and 0.27 THz as shown in Fig. 2f in accordance with the photoconduction routes (See Supplementary Fig. 5b in detail). In addition, the zero-bias photocurrent component ($I_{ph\text{-}CA}$ or $I_{ph\text{-}DB}$), shown in Fig. 2g, survives during these measurements, and demonstrates a sub-linear dependency of the zero-bias photocurrent on the power intensity, validating the effectiveness of the analogous photovoltaic mode. The experimental results shown in Figs. 1and 2 suggest that the intra-Dirac-band excitation enable the detection of low-energy photons below the bandgap energy (photocurrent $I_{ph} > 1$ μA, even up to 6 μA at RT as shown in Supplementary Fig. 5), owning to the stable non-equilibrium dynamics of the electronic collective system. In contrast, for a weak photocurrent

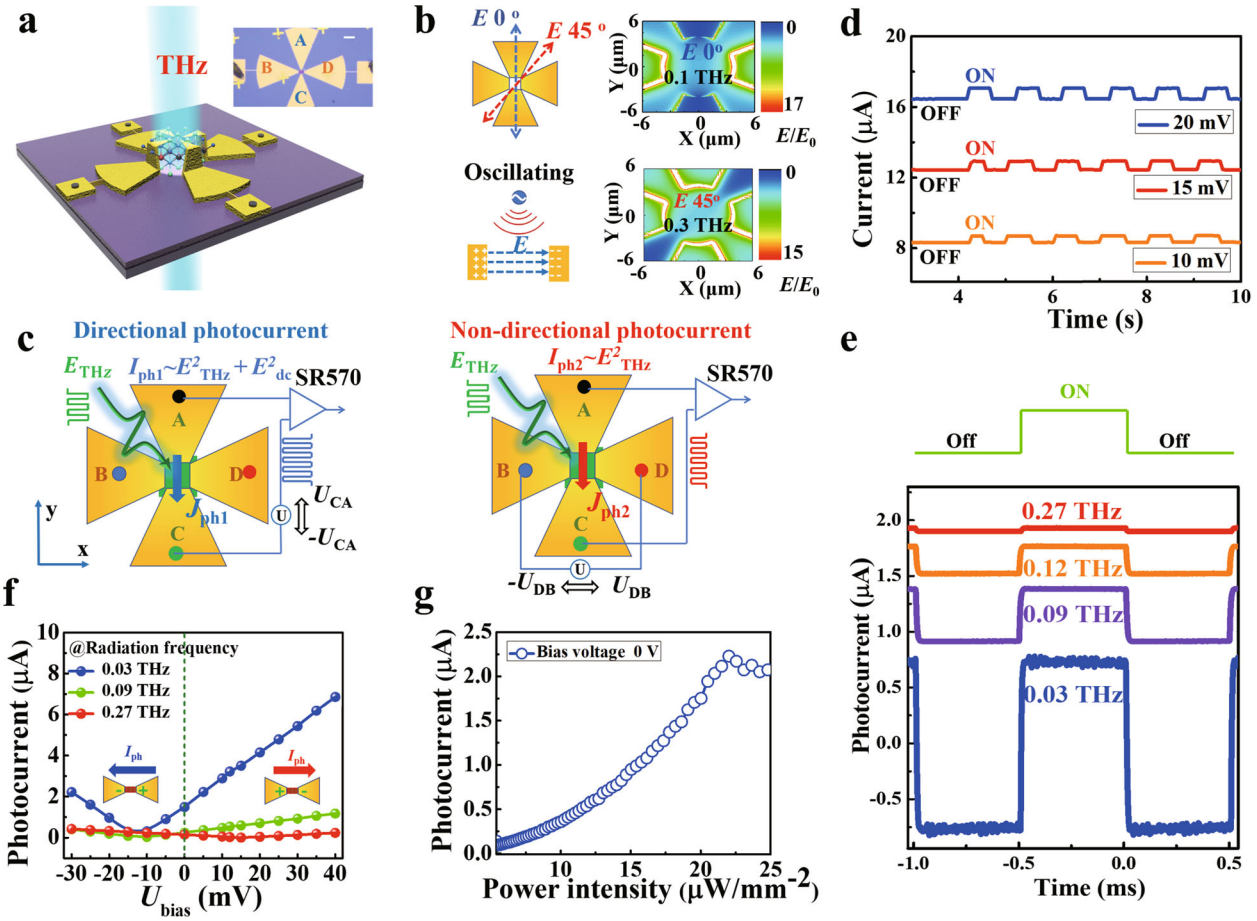

Fig. 2 The $EuSn_2As_2$ flakes-based THz detector and its photoresponse features. a Schematic illustration of the detector exploiting $EuSn_2As_2$ flakes integrated with multiple bow-tie antennas; inset: an optical micrograph image of the detector with the scale bar of 50 μm. **b** The FDTD simulations of the field distributions in the antenna gap at 0.1 and 0.3 THz radiation with incident polarization angles of 0° and 45°. Right side, the antenna-coupled incident electric field ratio E/E_0 onto the active area. **c** THz detection with two representative photocurrents (directional and non-directional photocurrents), where E_{THz} is the THz field, E_{dc} is the applied DC electric field and J_{ph} (J_{ph1} and J_{ph2}) is the photocurrent density. **d**, **e** Temporal photocurrent I_{ph} at bias voltage range of 10–30 mV and under 0.02–0.27 THz radiation; "ON" and "OFF" stand for illumination and no illumination, respectively. **f** Photocurrent ($I_{ph\text{-}CA}$ or $I_{ph\text{-}DB}$) as a function of the bias voltage U_{bias} (U_{CA} or U_{DB}) under 0.03 THz, 0.09 THz and 0.27 THz radiation. **g** Photocurrent (I_{ph}) as a function of the power density ($P_{density}$) at a zero-bias voltage.

(photocurrent $I_{ph} < 2$ nA at RT under a laser output power of 30 mW as indicated in Supplementary Fig. 3b) generated by visible and infrared photons, the intra-Dirac-band excitation is eliminated owing to the fast relaxation of the carriers before they reach the electrodes after the visible/infrared photoexcitation within a timescale of few femtoseconds to picoseconds[21].

Photoresponse controlling effects and non-equilibrium dynamics

Based on the above-mentioned analyses, it can be expected to occur that a net photocurrent flows in different directions and can be changed by tuning the applied voltage in the designed device. Its dominant dynamics depend on the following factors[22]: (i) the symmetry (or asymmetry) of the antenna and metal-materials contact; and (ii) the relative orientation between the electric field (or THz polarization) and the crystallographic axis of the material. Based on this, the photoelectric conversion process was vigorously evaluated via different designated strategies. "Strategy A" was designated to extrude the toggled phenomena stemming from the anisotropy of the crystallographic orientation as shown in Fig. 3a. Under the same THz polarization, the different linear behaviour of the photocurrent ($I_{ph\text{-}BA}$, $I_{ph\text{-}CA}$, $I_{ph\text{-}DA}$) with the sweeping voltage (U_{BA}, U_{CA}, U_{DA}) (because of the anisotropy of the orientation resistivity[23] as depicted in Supplementary Fig. 3a) is well preserved as shown in Fig. 3b, which conforms to the phenomenological explanation of photoconduction features. Based on this analysis, it can be concluded that directional photocurrent can be severely affected by combined effects of the non-equilibrium carriers' distribution and the orientation resistivity at different electrostatic contact points (electrode B, C, D). "Strategy B" was designed to examine the effect of boundary potential on the photoconduction phenomenon as shown in Fig. 3c. Under the same THz polarization and different bias voltage U_{BA} (10 mV, 0, and −10 mV), the sub-linear behaviour of the photocurrent ($I_{ph\text{-}BA}$) with the sweeping voltage (U_{CA}) from −8 mV to 8 mV, is evidently compensated by the photocurrent spilled over from the two bias voltages (U_{BA} and U_{CA}) as shown in Fig. 3d. Notably, the photoconduction is possibly affected by the following phenomena: (i) the boundary potential-induced changes in the THz field distribution or non-equilibrium carriers distribution (See Supplementary Fig. 3c for the peak response variation at different bias voltages), and (ii) the existence of two photosensitive areas ($S_{B\text{-}A}$ and $S_{C\text{-}A}$) that produce compensated photocurrents. "Strategy C" was designed to certify the non-equilibrium carriers' distribution induced by different THz polarizations as shown in Fig. 3e. Under the same bias voltage (U_{BA}) and without any boundary voltage, the THz-light polarization angle (θ) dependence of the photocurrent $I_{ph\text{-}BA}$ can be well fitted by a simple sine function ($I_{ph\text{-}BA}$ ~

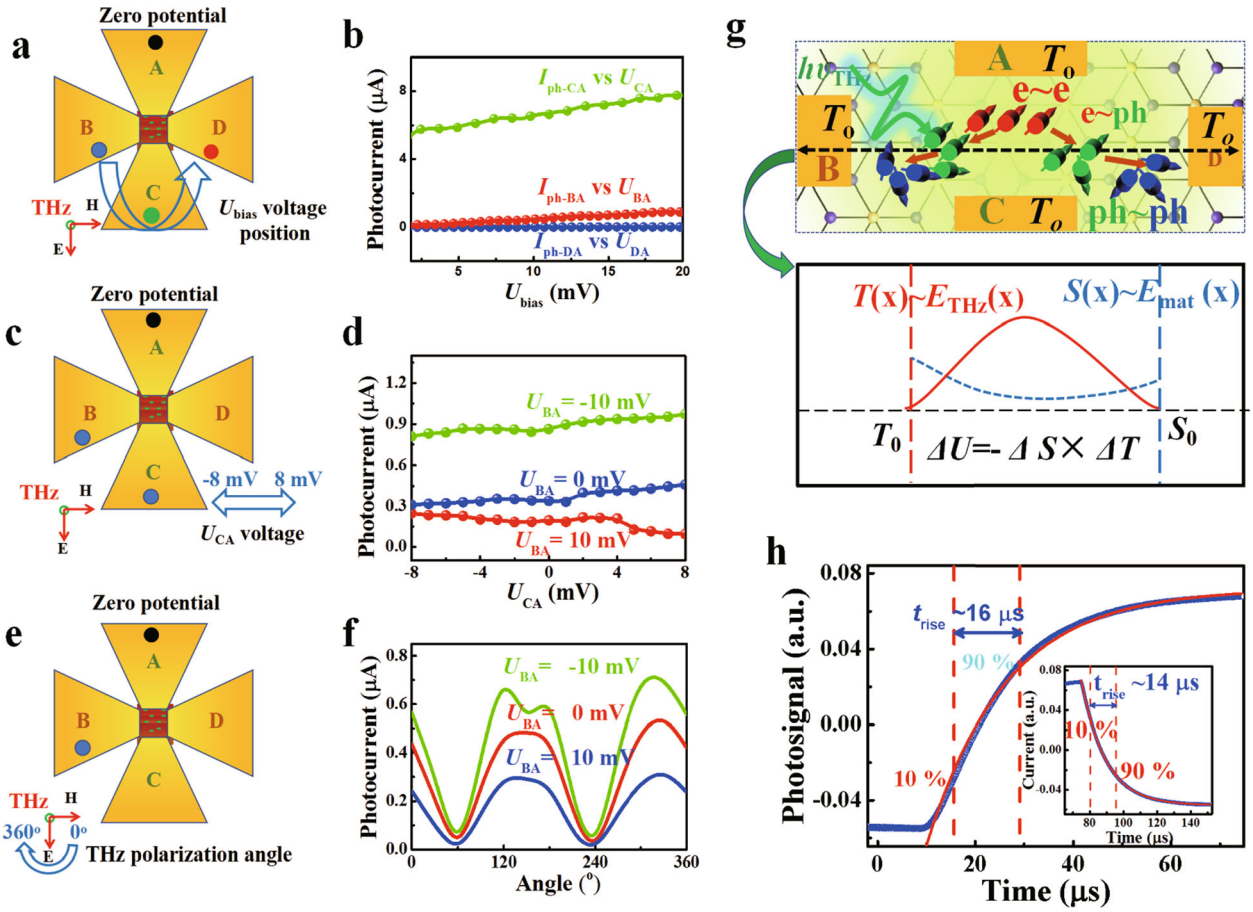

Fig. 3 Multi-dimensional controlling effects under 0.03 THz radiation. a, **b** Schematic and the photocurrents (I_{ph-BA}, I_{ph-CA}, I_{ph-DA}) were measured under a sweeping voltage, U_{bias} (U_{BA}, U_{CA}, U_{DA}), from 0 mV to 20 mV at different electrode positions. **c**, **d** Schematic and the photocurrent (I_{ph-BA}) was measured under a sweeping voltage, U_{CA}, from −8 mV to 8 mV at the same material orientation. **e**, **f** Schematic and the photocurrent (I_{ph-BA}) measured under a sweeping THz polarization angle (0° to 360°) at a certain voltage U_{BA} (−10 mV, 0 mV and 10 mV). **g** Proposed non-equilibrium carriers' transport under electromagnetic radiation: T_o is the reference temperature. Only the intraband free carrier (Drude) absorption can be generated at such a low-photon energy. $T_{materials} > T_{sink} \sim T_o$, where $T_{materials}$ is the temperature of the flakes, and T_{sink} is the temperature of the metal sink. **h** Time-resolved photoresponse showing the deducted response time, $\tau_{rise/fall}$ near 16 μs and 14 μs, with the fitting function: exp ($\pm t/\tau$).

$E_{THz}^2 \times \sin\theta$) as presented in Fig. 3f, revealing that the PTE effect-depends on the square of the electric field. Thus, the polarization-dependent photocurrents (I_{ph-CA} and I_{ph-BD}) are not caused by the accidental symmetry breaking, and show a π/2 phase-shift[24].

Based on the aforementioned design, analysis and experimental results, the operational principle of the fabricated detectors can be reasonably explained by the activated non-equilibrium dynamics of the intrinsic electronic system, and this tentative assignment comes with a few caveats. Owing to the free-carrier absorption predominantly induced by the intrinsic electronic system[17], the non-equilibrium carrier's temperature (ΔT_e), is higher than the lattice temperature (ΔT_L) and is not uniformly distributed owing to the higher thermal conductance of the metal contacts and the non-uniform polarized THz coupling when $EuSn_2As_2$ is impinged by the THz photons as shown in Fig. 3g. Therefore, a temperature gradient of $\nabla T_e(x, y)$ along 2D photosensitive area can be formed. In addition, stemming from the intermixing of the different nanoscale junctions, the $EuSn_2As_2$ layer thickness, and the metal–$EuSn_2As_2$ contact, the Seebeck coefficient, $S(x, y)$ ($S = -\pi^2 k_B^2 T d\sigma/dE_F/3e\sigma$ given by the Mott relation)[25] is not completely symmetric across the photosensitive region (See Supplementary Figs. 7 and 8 for asymmetric photoresponce caused by the non-uniform contact and impedance). Consequently, the diffusion of non-equilibrium carriers creates a potential gradient $\nabla U(x, y) = -\nabla S(x, y) \times \nabla T_e(x, y)$, and the total signal is the integral of $\nabla U(x, y)$ over the 2D photosensitive region. Based on this, the graphene-$EuSn_2As_2$ flakes-metal heterojunction device exhibits a large asymmetry, and a large photocurrent is expected to achieve a higher detection performance[26]. Apart from the explanation of non-equilibrium carriers-induced non-directional photocurrent as shown in Fig. 2c mentioned above, a rectification detection mechanism attributed to skew scattering due to the emergence of inherent chirality of the itinerant electrons in a time-reversal invariant but inversion-breaking system can also prevail[21]. Naively, the intriguing anisotropic properties may[15] influence the electron's trajectory under the condition of external excitation (low temperature or other factors), and this anisotropy combined with the chiral Bloch electrons induce skew scattering under both the crystal and electromagnetic fields[23]. The anisotropic scattering of the chiral Bloch electrons and pertinent second-order nonlinear response of $EuSn_2As_2$-based THz detectors possibly induce a non-directional photocurrent (similar to the scattering photocurrent produced by the Hall effect) in response to the THz field. Although the conclusive mechanisms for scattering origins remain elusive, these mechanisms are possibly responsible for the low-energy high-sensitivity photoresponse inherent to $EuSn_2As_2$ material. To better verify the existence of non-equilibrium carriers' processes in terms of response speed, the time-resolved photocurrent response was evaluated, which showed the response time $\tau_{rise/fall}$ near 16 μs and 14 μs with a fitting function of exp (t/τ) under 0.03 THz radiation (See Supplementary Figs. 6 and 7a for fast response and high signal-to-

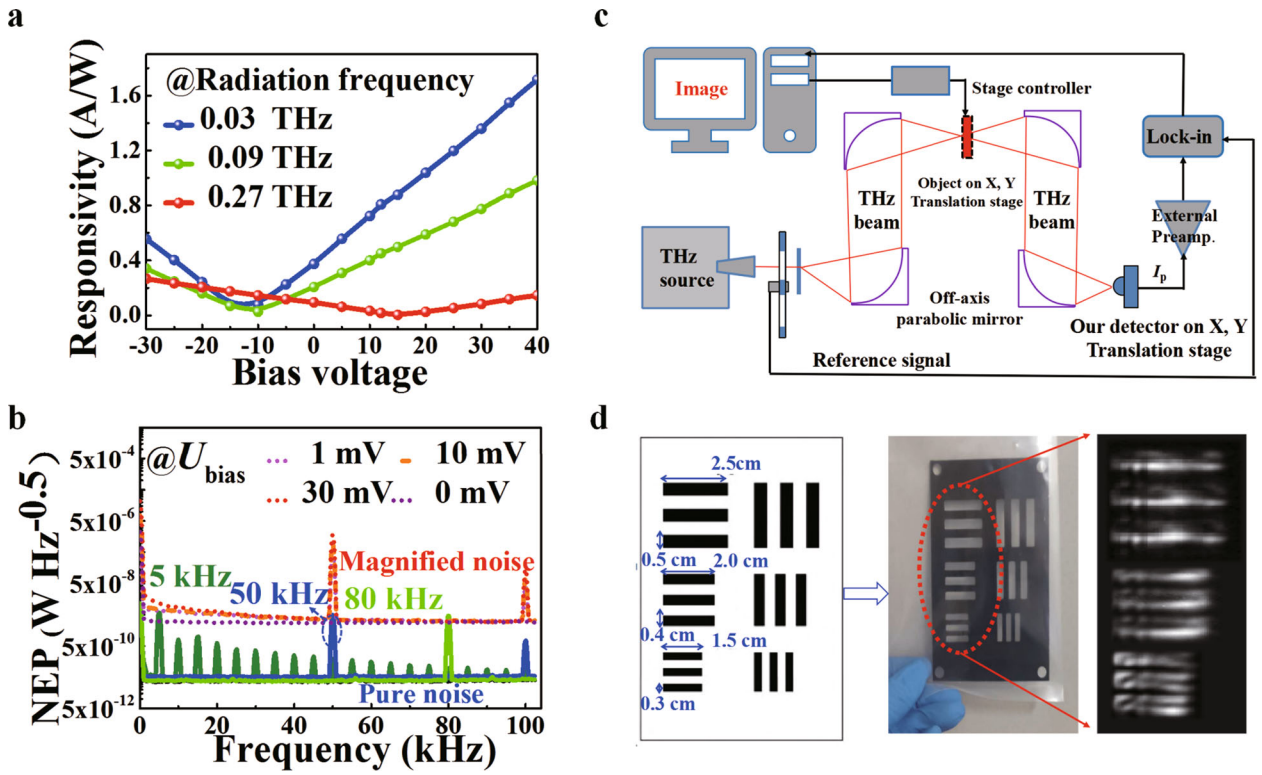

Fig. 4 Performance evaluation of $EuSn_2As_2$-based THz detectors. a Current responsivity as a function of bias voltage; input power $P_{in} \sim P_{density} \times S_{antenna}$; here, $S_{antenna} = \pi R^2 \sim 0.13\ mm^2$ is the whole area of the antenna, and $P_{density}$ is the power density reaching the detector. **b** NEP of the detector under the without/with modulated radiation (5 kHz, 50 kHz, and 80 kHz) and bias voltages (0 mV, 1 mV, 10 mV and 30 mV). The pure noise of a single device is indicated using the solid line ($U_{bias} = 0$ mV), and the magnified noise (>100 times) of single device and test system is indicated using the dotted line. **c** Schematic of transmission-mode THz imaging for macroscopic objects. **d** Image of a scale plate scanned at 0.27 THz in the single-pixel transmission mode.

noise ratio)[27–33]. Moreover, the fast photoresponse can be attributed to the absence of slow trapping-related carrier recombination owing to an intrinsic electronic system involving low-energy photons. Moreover, the static electric field accelerates the photo-excited carriers towards the electrodes quickly, thereby facilitating an efficient charge carriers' collection[8].

Detection performance and imaging application

Further, the performance of the detector in reference to the active structure-area rather than the $EuSn_2As_2$-material's area (See Supplementary Fig. 9 for high sensitivity by all-around calculated responsivity), was analyzed as well. The current responsivity $R_I =$ 0.2–1.6 A/W (cal. $R_v = 0.3$–2.4 kV/W) is observed to grow linearly with the bias voltage, even when the frequency is extended to 0.27 THz as shown in Fig. 4a, benefiting from the broadband absorption characteristics of the $EuSn_2As_2$ flakes, irrespective of the different coupling efficiency of the frequency-dependent antenna. A low noise-equivalent power (NEP) value of 30 pW/$Hz^{0.5}$ (pure noise) and 2 nW/$Hz^{0.5}$ (magnified noise about >100 times), without/with the bias voltage, is obtained via the noise spectral density measurements performed using a dynamic signal analyzer (SR785) as shown in Fig. 4b. The photoresponse of the fabricated detectors was found to be favourable even over a modulated frequency of 80 kHz, and is evidently faster than the currently available room-temperature thermal detectors with millisecond response times, substantiating the capability of the high signal-to-noise ratio (SNR) observed for the designed detectors (See Supplementary Figs. 6, 7a for fast response and high signal-to-noise). Finally, to further evaluate the application performance of a single-pixel detector at room temperature under an ambient environment, elaborate imaging experiments were devised as shown in Fig. 4c (See Supplementary Fig. 9d for transmission experiment results). For a 2D raster scanning imaging under 0.27 THz radiation with a 1 kHz repetition rate, the detector and the imaging object were placed at the THz beam focus, and 200 × 200 points of the object were acquired through a combination of pre-amplification and lock-in techniques. As evident from Fig. 4d, a resolution of the scale plate better than 0.3 cm is obtained, which is close to the diffraction limit of the optical system. More than 1 h was required to acquire the image using a non-optimized setup via mechanical scanning of the half-scale plate. The clearly resolved feature of the target objects indicates the feasibility of these detectors in applications such as quality controlling. The comparative survey of the emerging THz photodetectors built from different materials is shown in Table 1 from three calculated responsivities, and the real photoresponse performance of our device is appealing to engineer applications for large-area and fast imaging. Finally, major improvements can be envisioned by engineering various device architectures with improved efficiencies, such as reducing the losses due to coupling with THz radiation.

DISCUSSION

In summary, we have explored and experimentally validated terahertz detectors based on multiple antennas-coupled $EuSn_2As_2$ flakes, showing both high sensitivity and a fast response for multiple working modes. The controllable non-equilibrium carriers' transport in the intrinsic electronic system allows a highly sensitive direct THz detection with photoconductive and photovoltaic modes contributed from the non-equilibrium dynamics or self-driven scattering origin, rendering these nanodevices suitable for real-time and low-power consumption imaging at room

Table 1. Comparison of the latest reported emerging THz photodetectors.

Frequency [THz]	Responsivity [V/W]	NEP [W Hz$^{-1/2}$]	Mechanism	Normalization area (A_{norm})	Refs.
0.3–1	0.1, 10, 32, 764, 4 k	1100×10^{-12}, 3×10^{-12}	Plasma waves, PTE Ballistic & Tunnelling rectification	$\lambda^2/4$, $\lambda^2/4\pi$	Graphene [4, 27–30]
0.15–0.298	0.15	4×10^{-8} 1×10^{-9}	Plasma waves, PTE	$\lambda^2/4$	BP[31]
0.293	0.21	1.36×10^{-8}	PTE	$\lambda^2/4$	$Bi_2Te_{2.2}Se_{0.8}$[7]
0.12	475 A W^{-1}	3.6×10^{-13}	Photogalvanic & Photon-drag effect	material area	Bi_2Se_3[8]
0.17	27 k	2×10^{-13}	EIW	material area (300 μm^2)	Bi_2O_2Se[32]
0.12	1.4 k	10^{-11}	PTE	material area	$PtTe_2$/graphene[33]
0.02~0.30	0.2–1.6 A/W (0.3–2.4k) 6–20 A/W (9–30k)	30×10^{-12}	PTE, Anisotropic scattering	device area (0.13 mm^2), $\lambda^2/4$, material area (50.24 μm^2)	This work ($EuSn_2As_2$)

The normalization area A_{norm}, refers to the area to which the incident power was normalized: $P_{norm} = P_{in} \times A_{norm}/A_{focus}$. In our work, we use three normalization area A_{norm} to quantitatively analyze the responsivity, whereas the incident power was not normalized to any area, and the incident power was account for losses occurring in the unfocusing system.

temperature. The design and evaluation strategies proposed in this work pave the way to activate, probe and exploit the activity non-equilibrium dynamics of $EuSn_2As_2$-material for devising THz devices with tailorable performance through a combination of optimization methods, such as alternative structures integrated with metamaterials, and experimental techniques, such as polarization- and time-resolved angle-resolved photoemission spectroscopy[21,34]. These results are crucial to bring to fruition in the field of THz optoelectronics to enable large-area, fast imaging applications as well as high-speed wireless communication.

METHODS

Single-crystal growth and device fabrication

The $EuSn_2As_2$ crystals were was synthesized via melting Eu, Sn and As in a stoichiometric ratio of Eu: Sn: As (1.1: 20: 2) in an alumina crucible enclosed inside a quartz tube jacket, under 50 mTorr pressures, at temperature 850 °C for 12 h. Afterwards, the tube was cooled to 600 °C at a rate of 3 °C/h and the excess Sn was removed via centrifugation after reaching the temperature of 600 °C, and shiny hexagonal single crystals were obtained. Next, the multi-layered $EuSn_2As_2$ (~80 nm) was exfoliated using a blue Nitto tape onto a 300-nm thick SiO_2 substrate over a high resistance Si. The standard ultraviolet lithography technique was used to pattern the electrodes, followed by electron-beam evaporation of Cr/Au metal. The characteristics of the $EuSn_2As_2$ flakes were assessed via a combination of X-ray diffraction, optical microscopy, and AFM imaging.

THz detection and imaging

For THz detection, the device was uniformly illuminated with a chopped electronic source, and the open-circuit photovoltaic signal or the short-circuit photocurrent signal was detected after processing the initial signal generated by the device using a preamplifier, lock-in amplifier and high-speed sampling oscilloscope. The evolution of the photocurrent curves of the devices was also measured under the "ON/OFF" modulated radiation. The radiation frequency was tuned up to 0.12 THz (WR 9.0 Tripler ~ 7.5 μW mm^{-2}) and 0.24–0.29 THz (WR 2.8 Tripler ~ 10 μW mm^{-2}) using a multiplier (Virginia Diodes Inc.) connected to a microwave source emitting radiation frequency in the range of 0.02–0.04 THz (Agilent E8257D ~ 25 μW mm^{-2}). The power flux intensity was calibrated by a TK100 power meter. For imaging application, as shown in Fig. 4c, a 0.27 THz beam was focused on the detector using two pairs of off-axis parabolic mirrors, and the images were acquired via raster scanning of the object at the beam focus, consisting of 200 × 200 points with 100 ms integration time at every point.

DATA AVAILABILITY

The data that support the findings of this study are available from the corresponding author upon reasonable request.

Received: 23 November 2021; Accepted: 11 March 2022;
Published online: 08 April 2022

REFERENCES

1. Dhillon, S. et al. The 2017 terahertz science and technology roadmap. *J. Phys. D: Appl. Phys.* **50**, 043001 (2017).
2. Hafez, H. et al. Extremely efficient terahertz high-harmonic generation in graphene by hot Dirac fermions. *Nature* **561**, 507 (2018).
3. Giorgianni, F. et al. Strong nonlinear terahertz response induced by Dirac surface states in Bi_2Se_3 topological insulator. *Nat. Commun.* **7**, 11421 (2016).
4. Gayduchenko, I. et al. Tunnel field-effect transistors for sensitive terahertz detection. *Nat. Commun.* **12**, 543 (2021).
5. Guo, W. et al. Sensitive terahertz detection and imaging driven by the photo-thermoelectric effect in ultrashort-channel black phosphorus devices. *Adv. Sci.* **7**, 1902699 (2020).
6. Mittendorff, M., Winnerl, S. & Murphy, T. E. 2D THz optoelectronics. *Adv. Opt. Mater.* **9**, 2001500 (2020).
7. Viti, L. et al. Plasma-wave terahertz detection mediated by topological insulators surface states. *Nano Lett.* **16**, 80 (2016).
8. Tang, W. et al. Ultrasensitive room-temperature terahertz direct detection based on a bismuth selenide topological insulator. *Adv. Funct. Mater.* **28**, 1801786 (2018).
9. Cai, X. et al. Sensitive room-temperature terahertz detection via the photo-thermoelectric effect in graphene. *Nat. Nanotechnol.* **9**, 814 (2014).
10. Liu, J., Xia, F., Xiao, D., Javier García de Abajo, F. & Sun, D. Semimetals for high-performance photodetection. *Nat. Mater.* **19**, 830 (2020).
11. Wang, Y. et al. Ultrabroadband, sensitive, and fast photodetection with needle-like $EuBiSe_3$ single crystal. *ACS Photonics* **6**, 895 (2019).
12. Li, H. et al. Dirac surface states in intrinsic magnetic topological insulators $EuSn_2As_2$ and $MnBi_{2n}Te_{3n+1}$. *Phys. Rev. X* **9**, 41039 (2019).
13. Liu, E. et al. Giant anomalous Hall effect in a ferromagnetic Kagome-lattice semimetal. *Nat. Phys.* **14**, 1125 (2018).
14. Arguilla, M. Q. et al. $EuSn_2As_2$: an exfoliatable magnetic layered Zintl-Klemm phase. *Inorg. Chem. Front.* **4**, 378 (2017).
15. Gui, X. et al. A new magnetic topological quantum material candidate by design. *ACS Cent. Sci.* **5**, 900 (2019).
16. Chen, S. Q. et al. Broadband optical and microwave nonlinear response in topological insulator. *Opt. Mater. Express* **4**, 587 (2014).
17. Ogawa, N. et al. Zero-bias photocurrent in ferromagnetic topological insulator. *Nat. Commun.* **7**, 12246 (2016).
18. Li, G. et al. The localized near-field enhancement of metallic periodic bowtie structure: An oscillating dipoles picture. *Phys. B: Condens. Matter* **407**, 2223 (2012).

19. Seo, M. A. et al. Terahertz field enhancement by a metallic nano slit operating beyond the skin-depth limit. *Nat. Photonics* **3**, 152 (2009).
20. Isobe, H., Xu, S. & Fu, L. High-frequency rectification via chiral Bloch electrons. *Sci. Adv.* **6**, 2497 (2020).
21. Kastl, C., Karnetzky, C., Karl, K. & Holleitner, A. Ultrafast helicity control of surface currents in topological insulators with near-unity fidelity. *Nat. Commun.* **6**, 6617 (2015).
22. Viti, L., Politano, A. & Vitiello, M. S. Black phosphorus nanodevices at terahertz frequencies: photodetectors and future challenges. *APL Mater.* **5**, 035602 (2017).
23. Su, B. et al. Strong and tunable electrical anisotropy in type-II Weyl semimetal candidate WP_2 with broken inversion symmetry. *Adv. Mater.* **31**, 1903498 (2019).
24. Zhang, L. et al. High-frequency rectifiers based on type-II Dirac fermions. *Nat. Commun.* **12**, 1584 (2021).
25. Viti, L. et al. Efficient terahertz detection in black-phosphorus nano-transistors with selective and controllable plasma-wave, bolometric and thermoelectric response. *Sci. Rep.* **6**, 20474 (2016).
26. Guo, C. et al. Ultrasensitive ambient-stable $SnSe_2$-based broadband photodetectors for room-temperature IR/THz energy conversion and imaging. *2D Mater.* **7**, 035026 (2020).
27. Vicarelli, L. et al. Graphene field-effect transistors as room-temperature terahertz detectors. *Nat. Mater.* **11**, 865 (2012).
28. Bandurin, D. A. et al. Resonant terahertz detection using graphene plasmons. *Nat. Commun.* **9**, 5392 (2018).
29. Castilla, S. et al. Fast and sensitive terahertz detection using an antenna-integrated graphene pn junction. *Nano Lett.* **19**, 2765 (2019).
30. Auton, G. et al. Terahertz detection and imaging using graphene ballistic rectifiers. *Nano Lett.* **17**, 7015 (2017).
31. Viti, L. et al. Black phosphorus terahertz photodetectors. *Adv. Mater.* **27**, 5567 (2015).
32. Chen, Y. et al. Broadband Bi_2O_2Se photodetectors from infrared to terahertz. *Adv. Funct. Mater.* **31**, 2009554 (2021).
33. Xu, H. et al. $PtTe_2$-based type-II Dirac semimetal and Its van der Waals heterostructure for sensitive room temperature terahertz photodetection. *Small* **15**, 1903362 (2019).
34. McIver, J., Hsieh, D., Steinberg, H., Jarillo-Herrero, P. & Gedik, N. Control over topological insulator photocurrents with light polarization. *Nat. Nanotech.* **7**, 96 (2012).

ACKNOWLEDGEMENTS

This work was supported in part by the State Key Program for Basic Research of China (2018YFA0306200, 2017YFA0305500), the National Natural Science Foundation of China (Grant No. 61875223, 61875217, 91850208, 61991442, 61521005, and 62005249), the Zhejiang Provincial Natural Science Foundation (LQ20F050005) and Excellent Postdoctoral Research Projects of Zhejiang Province (ZJ2021019). We thank Westlake Center for Micro/Nano Fabrication for the facility support and technical assistance.

AUTHOR CONTRIBUTIONS

L.W. and X.S.C. conceived the project. Y.L. provided the photosensitive material. C.L., L.Z., and Z.C. designed the experiments. C.L., Y.L., Z.C., S.Z., and C.S. conducted all the experiments. C.L., G.L., and L.Z. undertook theoretical calculations. C.L. and L.W. participated in writing the manuscript. X.Y., Z.X., W.L., Y.L., and W.Z. analyzed the data. All authors contributed to the organization of the manuscript.

COMPETING INTERESTS

The authors declare no competing interests.

ADDITIONAL INFORMATION

Supplementary information The online version contains supplementary material available at https://doi.org/10.1038/s41699-022-00301-z.

Correspondence and requests for materials should be addressed to Xiaoshuang Chen or Lin Wang.

Reprints and permission information is available at http://www.nature.com/reprints

Publisher's note Springer Nature remains neutral with regard to jurisdictional claims in published maps and institutional affiliations.